A Cartesian relative motion approach to optimal formation flight using Lorentz forces and impulsive thrusting

Behrad Vatankhahghadim, Christopher J. Damaren [*]

University of Toronto Institute for Aerospace Studies, 4925 Dufferin Street, Toronto, Ontario, M3H 5T6, Canada

ARTICLE INFO

ABSTRACT

Hybrid combination of Lorentz forces and impulsive thrusts, provided by modulating spacecraft's electrostatic charge and propellant usage, respectively, is proposed for formation flight applications. A hybrid linear quadratic regulator, previously proposed in another work using a differential orbital elements-based model, is reconsidered for a Cartesian coordinates-based description of the spacecraft's relative states. In addition, the effects of adopting circular versus elliptic reference solutions on the performance of the controller are studied. Numerical simulation results are provided to demonstrate the functionality of the proposed controller in the presence of J_2 perturbations, and to illustrate the improvements gained by assuming an elliptic reference and incorporating auxiliary impulsive thrusts.

1. Introduction

Formation flight of spacecraft, involving groups of multiple satellites that orbit in proximity of each other, has seen a lot of renewed interest in recent years. This is particularly because of the improvements they offer over single-spacecraft missions in terms of affordability and robustness, and is facilitated by recent technological and scientific developments that enable reliable formation missions. One potential approach for spacecraft to achieve and maintain formation is via Lorentz-augmented control. The idea of using Lorentz forces generated by the interaction of actively-modulated charges on a spacecraft with the geomagnetic field in order to produce useful thrust was first proposed in Ref. [1].

In Ref. [2], analytical solutions of the equations of motion for Lorentz-augmented spacecraft in various situations were provided; however, only constant specific charges and circular reference frames were considered. The equations of motion linearized relative to a circular reference orbit were presented in Refs. [3,4], and are known as the Hill-Clohessy-Wiltshire (HCW) equations. Also using a spherical co-ordinates description similarly to [2], a three-spacecraft formation reconfiguration problem was considered in Ref. [5], but assuming proportional derivative-type feedback control provided by modulating the specific charge. Abandoning the circularity assumption on the chief spacecraft's orbit, Ref. [6] considered both circular and elliptic references using Cartesian coordinates for relative motion. In that work, step-wise charge control based on the linearized model, as well sequential

quadratic programming using the nonlinear model were proposed. The relative motion equations that allow for elliptic reference orbits are known as Tschauner-Hempel (TH) equations, and were provided in Refs. [7,8], among others.

In contrast to the use of spherical or Cartesian coordinates to describe the relative motion of spacecraft in formation, an alternative is to focus on the changes in the mean orbital elements, hence ignoring the short-term oscillations. Examples of past literature that make use of (mean) orbital elements (or their differences) for formation control are [9,10], and those of works that involve Lorentz-augmentation in particular are [11,12]. This approach is primarily motivated by the fact that, in many formation flight missions, only secular changes are of importance when determining tracking errors. While recognizing the value of this approach (especially in the presence of J_2 perturbations), the present authors have chosen to work directly with the Cartesian description of the spacecraft's absolute and relative positions. It is expected that such an approach will be better suited to applications for which short-term errors do matter. In order to demonstrate the effectiveness of the proposed controller and its comparability with the mean orbital elements-based techniques, J_2 influences are modelled in all simulation results to be presented. It is shown that the required specific charge and thrust magnitudes are still reasonable.

Hybrid formation control of spacecraft using continuous and impulsive forces in tandem is considered in this paper, based on a Cartesian coordinates-based model, and the methodology is applicable to both

circular and elliptic reference orbits for the chief spacecraft. The work presented in Ref. [6] considered the in-plane and out-of-plane motions separately when using the linearized model, and resorted to numerical approaches based on nonlinear trajectory design in order to treat more general cases with smaller errors. On the other hand, explicit expressions for the continuous and impulsive forces are presented in this document (although the associated Riccati equation still needs to be integrated numerically), and the complete three-dimensional motion is treated in a unified manner. The reference solution presented in Ref. [13] for elliptic orbits, in turn built upon the TH equations as presented in Ref. [8], are adopted in this work.

As demonstrated in Refs. [14,15] by studying the system's Gramian matrix, there is always one direction along which Lorentz-augmented formation is not controllable. This is because the Lorentz force is always perpendicular to the plane defined by the geomagnetic field vector and the spacecraft's velocity relative to the field. Similarly, controllability in the in-plane motion of equatorial reference orbits was demonstrated in Ref. [6], but out-of-plane motion was initially ignored in that analysis (and later on treated as uncontrolled drift). Motivated by a desire to overcome this controllability issue, the present work features a hybrid formulation that combines continuous-time Lorentz forces with impulsive thrusts, a problem that was treated in Refs. [12,14] based on a mean orbital elements-based model (as opposed to the current Cartesian formulation), as well as in Ref. [16]. As opposed to [16] that used trajectory optimization techniques and the pseudo-spectral method (followed by *a posteriori* distribution of the required control accelerations into continuous and impulsive contributions), the work described here uses a hybrid linear quadratic regulator (LQR) scheme based on that used in Refs. [12,14].

The primary rationale behind using LQR in the present work is that it is a well-established optimal control method that allows the user to trade off control effort against state errors. It also lends itself well to a hybrid formulation and the associated optimization, as delineated in the aforementioned references. Use of LQR in the context of formation flight was also seen in Ref. [17], assuming a discrete-time system and limiting the study to in-plane motion; in Ref. [18], using low-thrust continuous forces (not Lorentz forces) with circular reference orbits and accommodating gravitational disturbances; and in Ref. [19], also using continuous forces but allowing for the reference orbit's ellipticity.

The organization of this paper is as follows. A mathematical model of formation flight subject to Lorentz and thruster forces is constructed in Section 2 using relative motion equations in Cartesian coordinates. The hybrid LQR scheme to be used for control purposes is described in Section 3, along with circular and elliptic reference orbit solutions to be adopted. The functionality and performance of the proposed hybrid controller are demonstrated in Section 4 via numerical simulations, and the effects of reference orbit selection and incorporating auxiliary impulsive thrust on the performance are studied. Lastly, concluding remarks are made in Section 5.

2. Mathematical modelling of formation flight

This section establishes the mathematical model of the motion, to be used for control purposes in Section 3. The relationships that describe the geometry of motion are presented in Subsection 2.1, and the motion equations in the presence of applied forces are provided in Subsection 2.2.[1]

2.1. Kinematics

The following reference frames, illustrated in Fig. 1, are defined and used throughout the document:

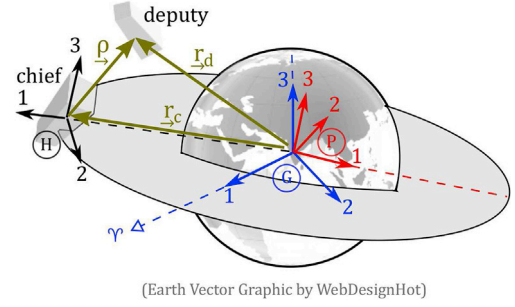(Earth Vector Graphic by WebDesignHot)

Fig. 1. Reference frames: (G) ECI, (P) perifocal, and (H) Hill.

- $\mathscr{F}_G$ – Earth-Centred Inertial (ECI) frame: origin at Earth's centre, 1-axis towards the vernal equinox, 3-axis towards Earth's North pole
- $\mathscr{F}_P$ – Perifocal frame: origin at Earth's centre, 1-axis towards the perigee of the chief's orbit, 3-axis normal to the chief's orbital plane
- $\mathscr{F}_H$ – Hill frame: origin at the chief's centre of mass, 1-axis pointing away from Earth's centre, 3-axis normal to the chief's orbital plane

The position vectors, measured from Earth's centre, of the chief and the deputy are given by $\vec{\mathbf{r}}_c$ and $\vec{\mathbf{r}}_d$, respectively, the components of which in the ECI frame are given by column matrices, $\mathbf{r}_{c,G}$ and $\mathbf{r}_{d,G}$. Rotation matrices can then be used to obtain their corresponding Hill frame representations:

$$\mathbf{r}_{c,H} = \mathbf{C}_{HG}\mathbf{r}_{c,G} \quad, \quad \mathbf{r}_{d,H} = \mathbf{C}_{HG}\mathbf{r}_{d,G} \tag{1}$$

where $\mathbf{C}_{HG}$ is the rotation matrix from $\mathscr{F}_G$ to $\mathscr{F}_H$ which can be evaluated, along with its rate of change, as follows [19]:

$$\mathbf{C}_{HG} = \left[\frac{\mathbf{r}_{c,G}}{|\mathbf{r}_{c,G}|} \quad \frac{\mathbf{h}_{c,G}^{\times}\mathbf{r}_{c,G}}{|\mathbf{h}_{c,G}^{\times}\mathbf{r}_{c,G}|} \quad \frac{\mathbf{h}_{c,G}}{|\mathbf{h}_{c,G}|} \right]^{\mathsf{T}} \tag{2a}$$

$$\dot{\mathbf{C}}_{HG} = \left[\frac{d}{dt}\left(\frac{\mathbf{r}_{c,G}}{|\mathbf{r}_{c,G}|}\right) \frac{d}{dt}\left(\frac{\mathbf{h}_{c,G}^{\times}\mathbf{r}_{c,G}}{|\mathbf{h}_{c,G}^{\times}\mathbf{r}_{c,G}|}\right) \frac{d}{dt}\left(\frac{\mathbf{h}_{c,G}}{|\mathbf{h}_{c,G}|}\right) \right]^{\mathsf{T}} \tag{2b}$$

where $\mathbf{h}_{c,G} = \mathbf{r}_{c,G}^{\times}\mathbf{v}_{c,G}$ denotes the ECI representation of the chief's orbital angular momentum vector. The derivatives in Eq. (2b) can be evaluated using the following identity for a generic $\mathbf{x}$:

$$\frac{d}{dt}\left(\frac{\mathbf{x}}{|\mathbf{x}|}\right) = \frac{\dot{\mathbf{x}}}{|\mathbf{x}|} - \frac{|\dot{\mathbf{x}}|}{|\mathbf{x}|^2}\mathbf{x} = \frac{\dot{\mathbf{x}}}{|\mathbf{x}|} - \frac{\mathbf{x}^{\mathsf{T}}\dot{\mathbf{x}}}{|\mathbf{x}|^3}\mathbf{x} \tag{3}$$

in conjunction with the following known relationships:

$$\frac{d}{dt}(\mathbf{r}_{c,G}) = \dot{\mathbf{r}}_{c,G} = \mathbf{v}_{c,G} \tag{4a}$$

$$\frac{d}{dt}(\mathbf{h}_{c,G}) = \dot{\mathbf{h}}_{c,G} = \mathbf{r}_{c,G}^{\times}\ddot{\mathbf{r}}_{c,G} = \mathbf{r}_{c,G}^{\times}\mathbf{f}_{p,G}(\mathbf{r}_{c,G}) \tag{4b}$$

$$\frac{d}{dt}\left(\mathbf{h}_{c,G}^{\times}\mathbf{r}_{c,G}\right) = \dot{\mathbf{h}}_{c,G}^{\times}\mathbf{r}_{c,G} + \mathbf{h}_{c,G}^{\times}\dot{\mathbf{r}}_{c,G} \tag{4c}$$

where $\mathbf{v}_{c,G}$ and $\mathbf{f}_{p,G}$ consist of the ECI components of the chief's absolute velocity vector and the perturbation forces (per unit mass) experienced by the chief. Lastly, noting that the spacecraft's relative position is given by $\boldsymbol{\rho} \triangleq \mathbf{r}_d - \mathbf{r}_c$, taking the difference of the position vectors in Eq. (1) and differentiating with respect to time yields:

$$\boldsymbol{\rho}_H = \mathbf{C}_{HG}\boldsymbol{\rho}_G \tag{5a}$$

$$\dot{\boldsymbol{\rho}}_H = \dot{\mathbf{C}}_{HG}\boldsymbol{\rho}_G + \mathbf{C}_{HG}\dot{\boldsymbol{\rho}}_G \tag{5b}$$

which will be used in simulation to obtain the relative states at each time.

2.2. Dynamics

The equations of motion that describe the system of interest's dynamics are given by Newton's law of gravitation:

$$\ddot{\mathbf{r}}_{c,G} = \frac{-\mu_e}{r_c^3}\mathbf{r}_{c,G} + \mathbf{f}_{p,G}(\mathbf{r}_{c,G}) \tag{6a}$$

$$\ddot{\mathbf{r}}_{d,G} = \frac{-\mu_e}{r_d^3}\mathbf{r}_{d,G} + \mathbf{f}_{p,G}(\mathbf{r}_{d,G}) + \mathbf{f}_{ct,G} + \mathbf{f}_{ds,G} \tag{6b}$$

where $r \triangleq |\mathbf{r}_G| = |\mathbf{r}_H|$ and $\mu_e = 3.986 \times 10^{14} \text{ m}^3/\text{s}^2$ is Earth's standard gravitational parameter, and spatial dependence of the perturbation force per unit mass, $\mathbf{f}_p$, is taken into account by representing it as a function of position. Assuming only the deputy is actuated, continuous- and discrete-time control forces per unit mass are denoted by $\mathbf{f}_{ct,G}$ and $\mathbf{f}_{ds,G}$, respectively. Subtracting Eq. (6b) from Eq. (6a) and using $\mathbf{r}_{d,G} = \boldsymbol{\rho}_G + \mathbf{r}_{c,G}$ by definition yields the following relative dynamics:

$$\ddot{\boldsymbol{\rho}}_G = -\frac{\mu_e(\boldsymbol{\rho}_G + \mathbf{r}_{c,G})}{|\boldsymbol{\rho}_G + \mathbf{r}_{c,G}|^3} + \frac{\mu_e}{r_c^3}\mathbf{r}_{c,G} + \left[\mathbf{f}_{p,G}(\boldsymbol{\rho}_G + \mathbf{r}_{c,G}) - \mathbf{f}_{p,G}(\mathbf{r}_{c,G})\right] + \mathbf{f}_{ct,G} + \mathbf{f}_{ds,G} \tag{7}$$

The primary perturbation source for spacecraft in formation is the J_2 perturbation resulting from the effects of Earth's non-spherical shape on its gravitational field [10,16]. An analytic expression for estimating the perturbation force, obtained by taking the gradient of the corresponding scalar field, is given by (as expressed in $\mathscr{F}_G$) [20]:

$$\mathbf{f}_{p,G} = \frac{3\mu_e J_2 R_e^2}{2|\mathbf{r}_G|^5}\left[\left(5\frac{(\mathbf{r}_G^\mathsf{T}\hat{\mathbf{g}}_3)^2}{|\mathbf{r}_G|^2} - 1\right)\mathbf{r}_G - 2(\mathbf{r}_G^\mathsf{T}\hat{\mathbf{g}}_3)\hat{\mathbf{g}}_3\right] \tag{8}$$

where $J_2 = 1.083 \times 10^{-3}$ for Earth represents the most dominant perturbation term associated with Earth's oblate shape, and $R_e = 6.378 \times 10^6$ m is Earth's radius. The unit column matrix, $\hat{\mathbf{g}}_3 = [0 \ 0 \ 1]^\mathsf{T}$, denotes the basis vector along the 3-axis of the ECI frame shown in Fig. 1, directed towards the North pole.

Lastly, the continuous- and discrete-time control forces per unit mass, assumed to be provided by the Lorentz force on the deputy caused by an actively-controlled accumulated charge, $\mathbf{q}(t)$, and impulsive thrusters, respectively, are given by (as expressed in $\mathscr{F}_G$):

$$\mathbf{f}_{ct,G}(t) = \frac{q}{m_d}\left(\cancelto{0}{\mathbf{E}_G} + \mathbf{v}_{rel,G}^\times \mathbf{b}_G\right) \approx -\hat{q}\mathbf{b}_G^\times\left(\mathbf{v}_{d,G} - \boldsymbol{\omega}_{e,G}^\times \mathbf{r}_{d,G}\right) \tag{9a}$$

$$\mathbf{f}_{ds,G}(t) = \sum_{k=1}^{\infty} \boldsymbol{\nu}_{k,G}\delta(t - t_k) \tag{9b}$$

where $\hat{q} \triangleq q/m_d$ is defined for specific charge per unit deputy mass, m_d, and $\mathbf{v}_{rel,G}$ represents the spacecraft's velocity relative to Earth's magnetic field. The electrical field strength, $\mathbf{E}_G$, is assumed to be negligible. In addition, $\boldsymbol{\omega}_{e,G} = 360.9856 \ \hat{\mathbf{g}}_3$ deg/s and $\mathbf{b}_G$ are the inertial components of Earth's angular velocity (about its own axis of rotation) and magnetic field vector (obtained upon assuming a tilted dipole model as described in Appendix H of [21]). The Dirac delta function, $\delta(t)$, centred at each

impulse time, t_k with $k \in \mathbb{N}$, is used in conjunction with gain values, $\boldsymbol{\nu}_k$, to represent three-dimensional impulsive thrust forces per unit mass.

3. Formation control

In preparation for application of the hybrid LQR scheme of [14] to the Cartesian formation flight problem in hand, the motion model of Section 2 is first linearized in Subsection 3.1. Two different, yet related, reference orbit solutions that assume circular or elliptic chief orbits (based on the HCW and TH equations, respectively) are selected in Subsection 3.2, and treating deviations from these solutions as relative state errors, Subsection 3.3 completes the description of the control scheme by determining the appropriate continuous and impulsive control inputs. It should be noted that both of these solutions are linearized and are expected to work well for small enough formations [13], but higher order solutions may be desired for large relative distances or highly elliptic reference orbits.

3.1. Linearized control system

The relative dynamics in Eq. (7) can be expressed in state-space form as a system of continuous- and discrete-time equations. To this end, assuming a circular orbit for the chief and linearizing Eq. (7) about this circular reference yields the following model as expressed in $\mathscr{F}_H$, based on the HCW equations in Refs. [3,4]:

$$\underbrace{\begin{bmatrix} \dot{\boldsymbol{\rho}}_H(t) \\ \ddot{\boldsymbol{\rho}}_H(t) \end{bmatrix}}_{\dot{\mathbf{x}}(t)} \approx \underbrace{\begin{bmatrix} 0_{3\times3} & 1_{3\times3} \\ \mathbf{M} & \mathbf{N} \end{bmatrix}}_{\mathbf{A}_{ct}} \underbrace{\begin{bmatrix} \dot{\boldsymbol{\rho}}_H(t) \\ \dot{\boldsymbol{\rho}}_H(t) \end{bmatrix}}_{\mathbf{x}(t)}$$
$$+ \underbrace{\begin{bmatrix} 0_{3\times1} \\ -\mathbf{C}_{HG}(t)\mathbf{b}_G^\times(t)\left(\mathbf{v}_{c,G}(t) - \boldsymbol{\omega}_{E,G}^\times\mathbf{r}_{c,G}(t)\right) \end{bmatrix}}_{\mathbf{B}_{ct}(t)} \underbrace{[\hat{q}]}_{u_{ct}(t)} \quad , \ t \neq t_k \tag{10a}$$

$$\underbrace{\begin{bmatrix} \boldsymbol{\rho}_H(t_k^+) \\ \dot{\boldsymbol{\rho}}_H(t_k^+) \end{bmatrix}}_{\mathbf{x}(t_k^+)} \approx \underbrace{\begin{bmatrix} 1_{3\times3} & 0_{3\times3} \\ 0_{3\times3} & 1_{3\times3} \end{bmatrix}}_{\mathbf{A}_{ds}} \underbrace{\begin{bmatrix} \boldsymbol{\rho}_H(t_k^-) \\ \dot{\boldsymbol{\rho}}_H(t_k^-) \end{bmatrix}}_{\mathbf{x}(t_k^-)} + \underbrace{\begin{bmatrix} 0_{3\times3} \\ 1_{3\times3} \end{bmatrix}}_{\mathbf{B}_{ds}} \underbrace{[\boldsymbol{\nu}_k]}_{\mathbf{u}_{ds,k}} \quad , \ t = t_k \tag{10b}$$

where the deputy-related quantities in Eq. (9a) are replaced by chief-related ones, consistent with the linearity assumption of $\mathbf{r}_{c,H} \approx \mathbf{r}_{d,H}$. In order to assess up to what relative distance is the assumption valid that $\mathbf{b}_G$ is the same at both chief and deputy locations, a numerical study was performed: the orbit-averaged value of $\max_{1\le i\le3}\{|\Delta\mathbf{b}_{G,i}/\mathbf{b}_{c,G,i}|\}$ was determined for the ith component of $\mathbf{b}_{c,G}$ and its variation, $\Delta\mathbf{b}_{G,i} \triangleq \mathbf{b}_{d,G,i} - \mathbf{b}_{c,G,i}$, over a circular region (in the hill frame's yz-plane) centred at the chief's location. Using the reference orbits considered in Section 4, the value of this metric does not exceed 1% for relative distances of less than 6 km.

The constant matrices $\mathbf{M}$ and $\mathbf{N}$ are given by:

$$\mathbf{M} = \begin{bmatrix} 3n^2 & 0 & 0 \\ 0 & 0 & 0 \\ 0 & 0 & -n^2 \end{bmatrix} , \quad \mathbf{N} = \begin{bmatrix} 0 & 2n & 0 \\ -2n & 0 & 0 \\ 0 & 0 & 0 \end{bmatrix} \tag{11}$$

where $n \triangleq (\mu_e/r_c^3)^{1/2}$ is the mean orbital motion of the chief.

3.2. Reference orbit

A special family of periodic solutions to Eq. (10a) for the uncontrolled case of $u_{ct} \equiv 0$, known as the Projected Circular Orbit (PCO) solution, is given by Ref. [22]:

$$\boldsymbol{\rho}_{ref,H} = \begin{bmatrix} \dfrac{R_{pco}}{2} \sin(nt + \alpha_0) \\ R_{pco} \cos(nt + \alpha_0) \\ R_{pco} \sin(nt + \alpha_0) \end{bmatrix} \tag{12}$$

where R_{pco} is the radius of the target PCO, and α_0 is the initial phase angle in the resulting circle. The corresponding relative velocity is obtained by differentiating Eq. (12) with respect to time:

$$\dot{\boldsymbol{\rho}}_{ref,H} = \begin{bmatrix} \dfrac{R_{pco}}{2} n \cos(nt + \alpha_0) \\ -R_{pco} n \sin(nt + \alpha_0) \\ R_{pco} n \cos(nt + \alpha_0) \end{bmatrix} \tag{13}$$

Provided in Ref. [13] is an extension of the above results to elliptic reference orbits, where the homogeneous solution to a linear time-varying set of equations analogous to the HCW equations in Eq. (10a) is provided. Selecting the integration constants in that expression in a certain way collapses it down to the following form [19]:

$$\boldsymbol{\rho}_{ref,H} = \begin{bmatrix} \dfrac{R_{pco}}{2} \cos(\theta) \\ -\dfrac{R_{pco}}{2} \sin(\theta) \left(\dfrac{2 + e\cos(\theta)}{1 + e\cos(\theta)} \right) \\ R_{pco} \left(\dfrac{\cos(\theta)}{1 + e\cos(\theta)} \right) \end{bmatrix} \tag{14}$$

where θ is the chief's true anomaly in its orbit, as measured in the perifocal reference frame, $\mathscr{F}_P$; and e is the chief orbit's eccentricity. The reader should note that setting $e = 0$ in Eq. (14) results in recovering the circular HCW solution in Eq. (12) with $\alpha_0 = \pi / 2$ selected. Differentiating Eq. (14) with respect to time yields:

$$\dot{\boldsymbol{\rho}}_{ref,H} = \begin{bmatrix} -\dfrac{R_{pco}}{2} \sin(\theta) \\ -\dfrac{R_{pco}}{2} \left(\cos(\theta) \dfrac{2 + e\cos(\theta)}{1 + e\cos(\theta)} + \dfrac{e\sin^2(\theta)}{[1 + e\cos(\theta)]^2} \right) \\ -R_{pco} \dfrac{\sin(\theta)}{[1 + e\cos(\theta)]^2} \end{bmatrix} \times \dfrac{h_c}{r_c^2} \tag{15}$$

where $h_c \triangleq |\mathbf{h}_c| = |\mathbf{r}_{c,G}^\times \mathbf{v}_{c,G}|$ and $r_c(\theta) \triangleq |\mathbf{r}_{c,G}(\theta)|$ are the magnitudes of the chief's orbital angular momentum, and position at true anomaly θ, respectively, and the relationship $\dot{\theta} = h_c/r_c^2$ (from Ref. [20], for instance) is used. Determining θ would require solving Kepler's equation at all times, which would be computationally expensive because of its nonlinear nature, and inaccurate because the perturbed orbits are no longer truly Keplerian. To circumvent these issues, the following relationships that are based on the polar description of osculating Keplerian orbits (tangent to the perturbed trajectory at the chief spacecraft's instantaneous location) are used:

$$\cos(\theta) = \dfrac{l - r_c}{e r_c} \tag{16a}$$

$$\sin(\theta) = \dfrac{l \mathbf{r}_{c,G}^\mathsf{T} \mathbf{v}_{c,G}}{e h_c r_c} \tag{16b}$$

where $l \triangleq a(1 - e^2)$ is the osculating orbit's semilatus rectum. The relative position and velocity solutions in Eqs. (14) and (15), in turn obtained using the trigonometric relations in Eq. (16), will be used in the following section as a reference (desired) trajectory for tracking purposes.

3.3. Hybrid LQR control

The hybrid LQR algorithm used in Ref. [14] (for mean orbital elements-based formation flight) is applied to the Cartesian position-based formation problem in hand. With the aim of tracking the (generally elliptical) reference orbit of Subsection 3.2, the state is taken to be the following Hill-frame error:

$$\mathbf{e}_H = \begin{bmatrix} \delta \boldsymbol{\rho}_H \\ \delta \dot{\boldsymbol{\rho}}_H \end{bmatrix} \triangleq \begin{bmatrix} \boldsymbol{\rho}_H - \boldsymbol{\rho}_{ref,H} \\ \dot{\boldsymbol{\rho}}_H - \dot{\boldsymbol{\rho}}_{ref,H} \end{bmatrix} \tag{17}$$
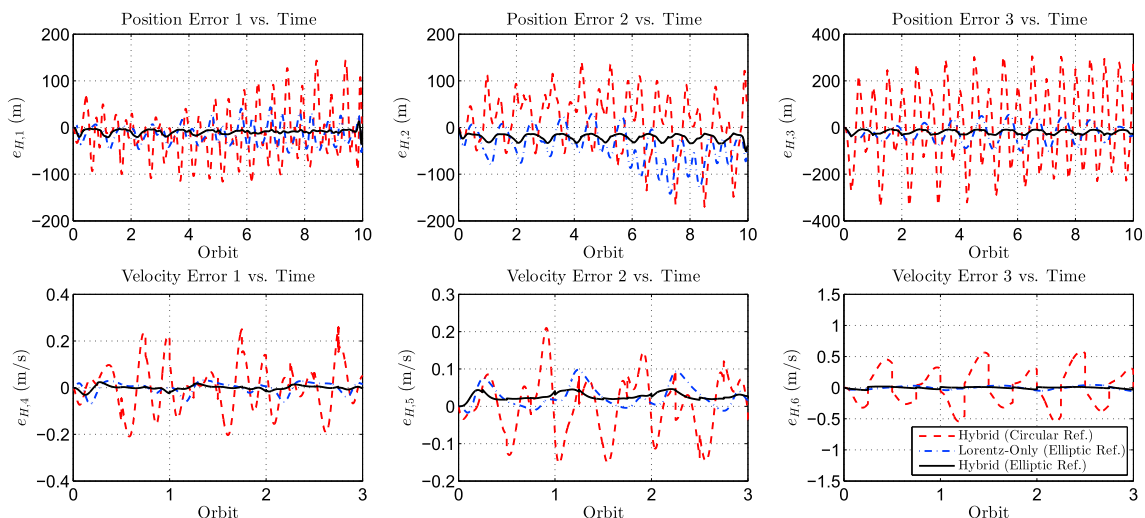

Fig. 2. Relative State Errors without Initial Off-set: 4-Impulse Hybrid with Circular Ref. (red dashed), Lorentz-Only with Elliptic Ref. (blue dash-dotted), and 4-Impulse Hybrid with Elliptic Ref. (black solid). (For interpretation of the references to colour in this figure legend, the reader is referred to the web version of this article.)
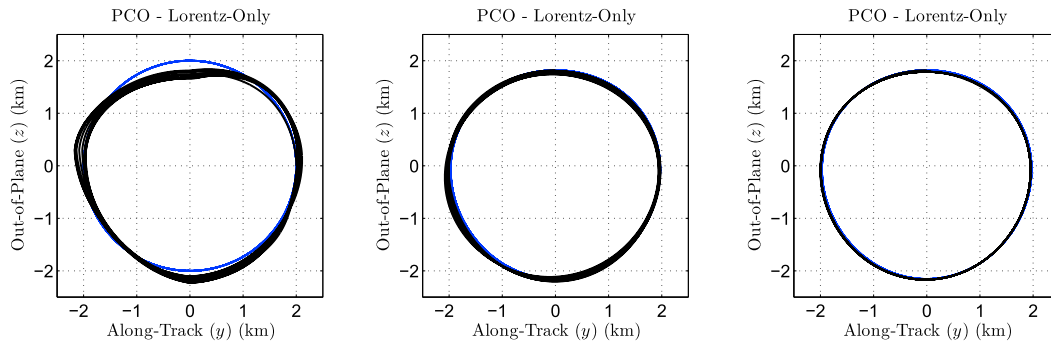
Fig. 3. PCO tracking performance without initial off-set: 4-Impulse hybrid with circular ref. (Left), Lorentz-only with elliptic ref. (Centre), and 4-impulse hybrid with elliptic ref. (Right).

where $\boldsymbol{\rho}_{ref,H}$ and $\dot{\boldsymbol{\rho}}_{ref,H}$ are given by Eqs. (12) and (13), or by Eqs. (14) and (15), depending on the controller. In addition, $\boldsymbol{\rho}_H$ and $\dot{\boldsymbol{\rho}}_H$ are the measured relative distance and velocities, assumed to be measurable by the spacecraft (via inter-satellite range sensing, for example). For simulation purposes, the time evolution of these variables is obtained by numerical integration of the nonlinear equation in Eq. (7) and the result's ECI-to-Hill frame transformation via Eq. (2), with $\mathbf{C}_{HG}$ given in Eq. (2a). However, even though full nonlinear simulations will be performed, the control scheme to be described below is based on the linearized model of Subsection 3.1.

Similarly to [14], the following hybrid cost function is defined, where the term "hybrid" refers to the variable's consisting of both continuous- and discrete-time costs:

$$\mathscr{I} = \frac{1}{2}\mathbf{e}^{\mathsf{T}}(t_f)\mathbf{S}\mathbf{e}(t_f) + \frac{1}{2}\int_0^{t_f}\left(\mathbf{e}^{\mathsf{T}}(t)\mathbf{Q}_{ct}\mathbf{e}(t) + R_{ct}u_{ct}^2(t)\right)\,dt \\ + \sum_{k=1}^N\left(\mathbf{e}^{\mathsf{T}}(t_k^-)\mathbf{Q}_{ds}\mathbf{e}(t_k^-) + \mathbf{u}_{ds,k}^{\mathsf{T}}\mathbf{R}_{ds}\mathbf{u}_{ds,k}\right) \quad (18)$$

where t_f is the terminal time. The matrix $\mathbf{S} = \mathbf{S}^{\mathsf{T}} \geq 0$ relates to the terminal state penalty; $\mathbf{Q}_{ct} = \mathbf{Q}_{ct}^{\mathsf{T}} > 0$ and $R_{ct} > 0$ are for the continuous-time state and (scalar) control penalties, respectively; and $\mathbf{Q}_{ds} = \mathbf{Q}_{ds}^{\mathsf{T}} > 0$ and $\mathbf{R}_{ds} = \mathbf{R}_{ds}^{\mathsf{T}} > 0$ scale the discrete-time state and control penalties, respectively. Minimizing the cost function in Eq. (18) eventually yields the following set of continuous- and discrete-time Riccati equations [14]:

$$\dot{\mathbf{P}}(t) = -\left[\mathbf{P}(t)\mathbf{A}_{ct} + \mathbf{A}_{ct}^T\mathbf{P}(t) - \mathbf{P}(t)\mathbf{B}_{ct}(t)R_{ct}^{-1}\,\mathbf{B}_{ct}^T(t)\mathbf{P}(t) + \mathbf{Q}_{ct}\right] \;,\; t{\neq}t_k \\ \mathbf{P}(t_f) = \mathbf{S} \quad (19a)$$

$$\mathbf{P}(t_k^-) = \mathbf{Q}_{ds} + \mathbf{P}(t_k^+) - \mathbf{P}(t_k^+)\mathbf{B}_{ds}\left[\mathbf{R}_{ds} + \mathbf{B}_{ds}^T\mathbf{P}(t_k^+)\mathbf{B}_{ds}\right]^{-1}\mathbf{B}_{ds}^T\mathbf{P}(t_k^+) \;,\; t = t_k \quad (19b)$$

which can be computed and stored beforehand by integrating Eq. (19a) backwards in time, starting from the terminal condition, and applying jumps in the resulting Riccati solution at every impulse time, t_k, based on Eq. (19b). The optimal continuous- and discrete-time feedback control inputs are then obtained by Ref. [14]:

$$u_{ct}^*(t) = \frac{q}{m_d} = -R_{ct}^{-1}\mathbf{B}_{ct}^T(t)\mathbf{P}(t)\mathbf{e}(t) \quad (20a)$$

$$\mathbf{u}_{ds,k}^* = \boldsymbol{\nu}_k = -\mathbf{R}_{ds}^{-1}\mathbf{B}_d^T\mathbf{A}_{ds}^{-T}\left[\mathbf{P}(t_k^-) - \mathbf{Q}_{ds}\right]\mathbf{e}(t_k^-) \quad (20b)$$

the determination of which completes the hybrid control scheme by dictating how the accumulated specific charge and thruster gains should be varied over time. It should be clarified that, having computed $\mathbf{P}(t)$ prior to the mission, its values can be stored and extracted with no need for on-board integration.

4. Numerical simulations

The orbital and control parameters selected for most of the simulations, as well as the relevant procedure are described in Subsection 4.1. The simulation results and the corresponding discussions are then provided in the subsequent sections, involving simulations without and with initial off-set in Subsections 4.2 and 4.3, as well as a comparison with past literature (namely [14]) in Subsection 4.4.

4.1. Simulation set-up and procedure

MATLAB® is used to test the performance of the proposed hybrid formation tracking controller. The chief spacecraft's initial orbital parameters are used to obtain the initial conditions on the chief's position and velocity, $\mathbf{r}_{c,G,0}$ and $\mathbf{v}_{c,G,0}$, and are also assumed by two of the controllers during the backward integration of Eq. (19). The remaining controller assumes a circular orbit with $e = 0$. All control schemes require an estimation of position and velocity (by solving Kepler's equation) in order to calculate $\mathbf{B}_c(t)$, from the linearized model in Eq. (10), via estimating the magnetic field vector, $\mathbf{b}_G(t)$ (assumed to be the same at both chief and deputy locations).

The continuous-time Riccati equation in Eq. (19a) is integrated backwards, starting from $\mathbf{P}(t_f) = \mathbf{S}$, and at each impulse time, $t = t_k$, jumps are induced in the solution based on the discrete-time equation in Eq. (19b). The obtained solution is then stored and used during forward simulation to determine the control inputs. Denoting the deputy's initial off-set from the intended PCO as $\delta\boldsymbol{\rho}_{H,0}$ and $\delta\dot{\boldsymbol{\rho}}_{H,0}$, the initial relative Hill frame states are set to $\boldsymbol{\rho}_{H,0} = \boldsymbol{\rho}_{H,ref}(0) + \delta\boldsymbol{\rho}_{H,0}$ and $\dot{\boldsymbol{\rho}}_{H,0} = \dot{\boldsymbol{\rho}}_{H,ref}(0) + \delta\dot{\boldsymbol{\rho}}_{H,0}$. The corresponding reference values are determined using Eqs. (12) and (13), or using Eqs. (14) and (15), depending on the controller. The deputy's initial conditions in Cartesian coordinates are then set to $\mathbf{r}_{d,H,0} = \mathbf{r}_{c,G,0} + (\mathbf{C}_{GH}\boldsymbol{\rho}_{H,0})$ and $\mathbf{v}_{d,H,0} = \mathbf{v}_{c,G,0} + (\mathbf{C}_{GH}\dot{\boldsymbol{\rho}}_{H,0} + \dot{\mathbf{C}}_{GH}\boldsymbol{\rho}_{H,0})$, where the inverse of Eq. (5) is used.

The complete nonlinear dynamics in Eq. (6) are integrated using a fixed-step fourth order Runge-Kutta algorithm, RK4, with a step size of $h = 0.1$ s. At each integration time step, a reverse procedure is used to obtain the relative states in the Hill frame; that is, Eq. (5) is evoked to obtain the relative states in $\mathscr{F}_H$ using the knowledge of the chief's and deputy's position and velocity (available via integration). The error variable in Eq. (17) is then evaluated by subtracting the reference solution and its rate, provided by Eqs. (12) and (13), or Eqs. (14) and (15), depending on the controller. Lastly, the computed error is used, in conjunction with the $\mathbf{P}(t)$ solution available via backward integration, to compute and apply the optimal control inputs given by Eq. (20), subsequently producing forces as described by Eq. (9).

4.2. Formation maintenance performance

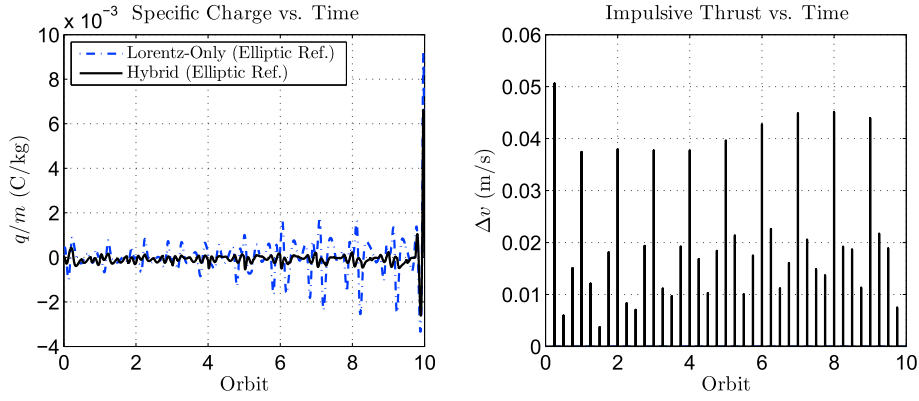The orbit considered in this subsection has the following parameters:

Fig. 4. Estimation of Electrostatic Charge and Thrust Δv Required without Initial Off-Set: Lorentz-Only with Elliptic Ref. (blue dash-dotted) and 4-Impulse Hybrid with Elliptic Ref. (black solid). (For interpretation of the references to colour in this figure legend, the reader is referred to the web version of this article.)

$$\{a, e, i, \omega, \Omega, t_0\} = \{7092 \text{ km}, 0.1, 0 \text{ rad}, \pi/4 \text{ rad}, \pi/4 \text{ rad}, 0 \text{ s}\}$$

The terminal penalty for the LQR is set to $\mathbf{P}(t_f) = \mathbf{S} = 10^6 \times \mathbf{1}_{6\times6}$. The continuous-time penalty variables, used for all controllers considered in this subsection, are set to $\mathbf{Q}_{ct} = blockdiag\{10^2 \times \mathbf{1}_{3\times3}, 10^5 \times \mathbf{1}_{3\times3}\}$ and $R_{ct} = 10^{10}$; while the discrete-time penalties, pertinent to the hybrid controller that incorporate impulsive thrusts, are tuned to be $\mathbf{Q}_{ds} = blockdiag\{10^2 \times \mathbf{1}_{3\times3}, 10^5 \times \mathbf{1}_{3\times3}\}$ and $\mathbf{R}_{ds} = 10^{10} \times \mathbf{1}_{3\times3}$.

Shown in Fig. 2 are the relative position and velocity tracking errors (in $\mathscr{F}_H$) over 10 orbits, starting with no initial off-set ($\delta\boldsymbol{\rho}_{H,0} = \delta\dot{\boldsymbol{\rho}}_{H,0} = 0$) and using three controllers: a four-impulse hybrid controller (red dashed) that assumes a circular reference orbit, a Lorentz-only controller with no impulses (blue dash-dotted) that assumes an elliptic reference orbit, and a four-impulse hybrid controller (black solid) that also assumes an elliptic reference. For the hybrid cases, the impulses are applied in intervals of $T/4$ starting from $t = 0$. Fig. 3 shows the resulting tracking performance as viewed along the x-direction, in the plane in which a PCO of radius $R_{pco} = 2$ km is desired. As evident from both figures, for the elliptic orbit considered and using the current set of penalties, the formation control performance is significantly enhanced by using the elliptic correction to the HCW equations, and further improvements ensue by incorporating impulses via the proposed hybrid algorithm.

Fig. 4 shows how much resources (electrostatic charge and thrust Δv) are expected to be required for the Lorentz-only and hybrid cases that use elliptic references, both of which are feasible with current technologies, considering a generally-acceptable range of $10^{-2} - 10^{-3}$ C / kg for specific charge [1,5]. As evident from this figure, reductions in specific charge ensue from incorporating impulses, of course at the cost of fuel consumption. The reader should not be alarmed by the increasing values of the resources required while approaching 10 orbits, as this does not suggest instability: the periodicity of the system (considering its magnetic field variations using the current orbital elements) is 14 orbits, and a similar beat-like pattern repeats with this period. Bounded motions were verified for even as long as 20 orbits. Part of this sudden increase is also

due to the Riccati solution deviating from its steady-state pattern and approaching the user-specified terminal value, $\mathbf{S}$.

Presented in Table 1 are some performance measures that, in addition to the total cost, $\mathscr{J}$ (defined in Eq. (18)), also include some root mean squared (RMS) norms defined generically as $\| \mathbf{x} \|_{10T} \triangleq \sqrt{\left(\int_0^{10T} \mathbf{x}^{\mathsf{T}} \mathbf{x} \, dt\right)/(10T)}$ for continuous variables, such that $\mathbf{x}$ is set to $\mathbf{f}_{ct}, \delta\boldsymbol{\rho}_H$, and $\delta\dot{\boldsymbol{\rho}}_H$ for specific continuous force, relative position error, and relative velocity error, respectively. Similarly, $\| \hat{q} \|_{10T} \triangleq \sqrt{\int_0^{10T} \left(\hat{q}(t)^2 \, dt\right)/(10T)}$ denotes the RMS of the specific charge. For the impulsive force measure, an analogous discrete-time parameter is defined as $\| \mathbf{f}_{ds} \|_{10T} \triangleq \sqrt{\left(\sum_{k=1}^N \mathbf{v}_k^{\mathsf{T}} \mathbf{v}_k\right)/N}$. Table 1 shows more than 75% and 57% reduction in the hybrid cost and relative position/velocity errors, respectively, as a result of adding impulsive thrusts. In addition, about 47% reduction is observed in the specific charge RMS as a consequence.

4.3. Transient behaviour with initial off-set

As mentioned in Section 1, the main motivation for using impulsive thrusts as an auxiliary mechanism to complement the Lorentz force-based formation control is overcoming the controllability issue associated with the latter. This is illustrated in Figs. 5 and 6 that show the relative state errors and resource consumption expected from using the same Lorentz-only and four-impulse hybrid controllers as described in Subsection 4.2 (with the same penalties and orbital parameters), but now with a non-zero initial condition; i.e. an initial off-set of $\delta\boldsymbol{\rho}_0 = [0.2 \ 0.2 \ 0.2]$ km and $\delta\dot{\boldsymbol{\rho}}_{H,0} = 0$ away from the desired PCO. As expected, the Lorentz-only controller suffers significantly owing to its lack of controllability in one direction at all times, whereas the hybrid controller is capable of eliminating the initial error and achieving the intended PCO formation. The reader should keep in mind that the thrust Δv could be reduced if need be, by more heavily penalizing the impulsive control effort via increasing $\mathbf{R}_{ds}$.

4.4. Comparison with previous results

In order to validate the results presented thus far and assess the performance of the proposed controller against those previously presented in literature, comparison is made against the simulation results of [14] (the control scheme of which was used in the present project). The following parameters based on the mean orbital elements used in Ref. [14] are selected to allow for a meaningful comparison:

Table 1
Performance, without initial off-set, of 4-impulse hybrid with circular ref., Lorentz-only with elliptic ref., and 4-impulse hybrid with elliptic ref. Controllers over 10T.

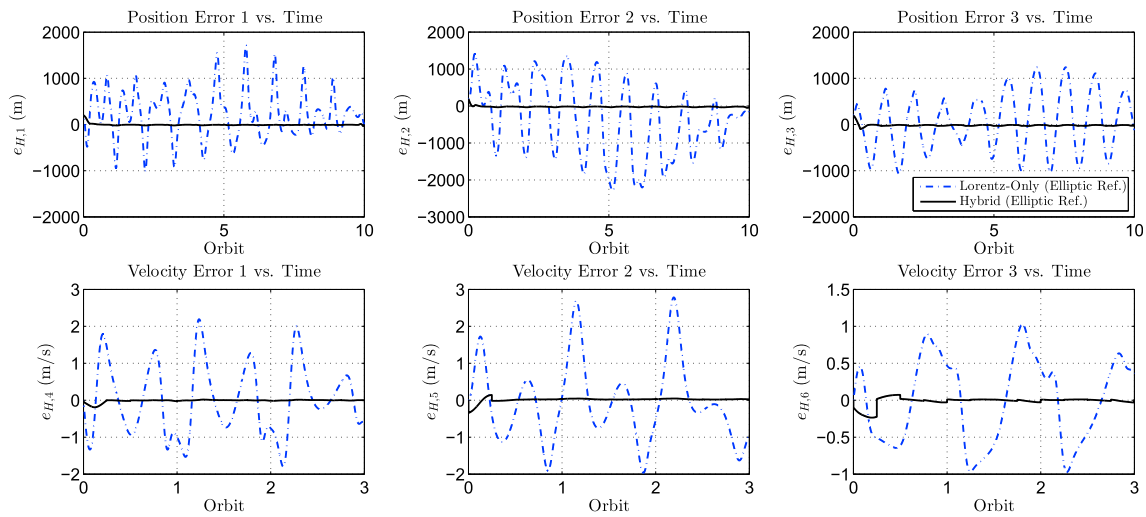| Param.	Description	4-Imp. Circ.	Lorentz	4-Imp. Ellip.	Unit
$\mathscr{J}_{10T}$	hybrid cost	1.92×10^{11}	1.91×10^{10}	4.50×10^9	–
$\hat{q}_{10T}$	specific charge	3.91×10^{-3}	8.67×10^{-4}	4.61×10^{-4}	C/kg
$\| \mathbf{f}_{ct} \|_{10T}$	Lorentz	6.06×10^{-4}	1.73×10^{-4}	1.01×10^{-4}	N/kg
$\| \mathbf{f}_{ds} \|_{10T}$	impulse	4.78×10^{-1}	0	2.47×10^{-2}	N·s/kg
$\| \delta\boldsymbol{\rho}_H \|_{10T}$	position error	1.81×10^2	7.56×10^1	3.21×10^1	m
$\| \delta\dot{\boldsymbol{\rho}}_H \|_{10T}$	velocity error	3.87×10^{-1}	8.45×10^{-2}	3.60×10^{-2}	m/s

Fig. 5. Relative State Errors with Non-Zero Off-set: Lorentz-Only with Elliptic Ref. (blue dash-dotted), and 4-Impulse Hybrid with Elliptic Ref. (black solid). (For interpretation of the references to colour in this figure legend, the reader is referred to the web version of this article.)

Fig. 6. Estimation of Electrostatic Charge and Thrust Δv Required with Non-Zero Initial Off-set: Lorentz-Only with Elliptic Ref. (blue dash-dotted) and 4-Impulse Hybrid with Elliptic Ref. (black solid). (For interpretation of the references to colour in this figure legend, the reader is referred to the web version of this article.)
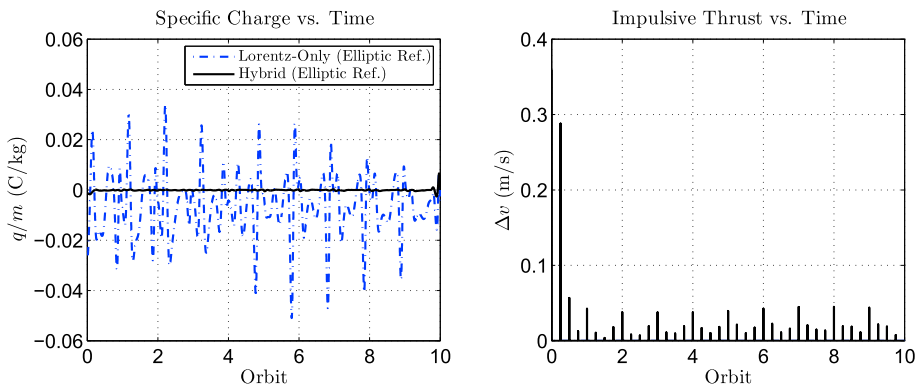
$$\{a, e, i, \omega, \Omega, t_0\} = \{7092 \text{ km}, 0.05, \pi/2 \text{ rad}, 0 \text{ rad}, \pi \text{ rad}, 0 \text{ s}\}$$

A PCO of $R_{pco} = 1$ km with no initial deputy off-set is chosen as the formation objective. The LQR parameters are set to $\mathbf{P}(t_f) = \mathbf{S} = blockdiag\{10^6 \times 1_{3\times3}, 10^{10} \times 1_{3\times3}\}$, $R_{ct} = 10^{13}$, and $\mathbf{R}_{ds} = 10^{11} \times 1_{3\times3}$. The state penalties are selected as suggested by Ref. [14], setting $\mathbf{Q}_{ct} = 10^5(\boldsymbol{\Xi}_{nz}\boldsymbol{\Xi}_{nz}^{\mathrm{T}})$ and $\mathbf{Q}_{ds} = 4 \times 10^{11}(\boldsymbol{\Xi}_z\boldsymbol{\Xi}_z^{\mathrm{T}})$. The matrices $\boldsymbol{\Xi}_{nz}$ and $\boldsymbol{\Xi}_z$ consist of the eigenvectors respectively corresponding to the non-zero eigenvalues and the smallest (close to zero) eigenvalue (related to the uncontrollable direction) of the controllability Gramian of the continuous-time portion of the system, namely Eq. (10a).

Simulation results obtained over 10 orbits (where steady-state is reached) using twenty impulses per orbit (every $T/20$, starting from

$t = T/40$) are partly presented in Fig. 7 and compared in Table 2 against some values from Ref. [14]. The parameters $|e_{H,i}|_{max}$ represent the largest magnitude of the error in the ith component of relative position. The averaged parameter $|\Delta v|_{avg}/\text{orb}$ denotes the mean of $|\boldsymbol{v}_k|$ times the number of impulses per orbit, and $\| \hat{q} \|_{10T}$ as defined in Table 1 is an RMS measure of the specific charge (assuming RMS of the results in Ref. [14] does not change much when going from 10 orbits to 100 as reported in that paper). The errors and specific charge required are comparable with or better than those of [14] overall, despite using a Cartesian coordinates-based approach here instead of mean orbital elements, but the latter is clearly superior in terms of fuel consumption. In addition, Fig. 7 (compared to Fig. 2 that features errors in the order of 20–40 m using four impulses) demonstrates that arbitrarily small tracking errors
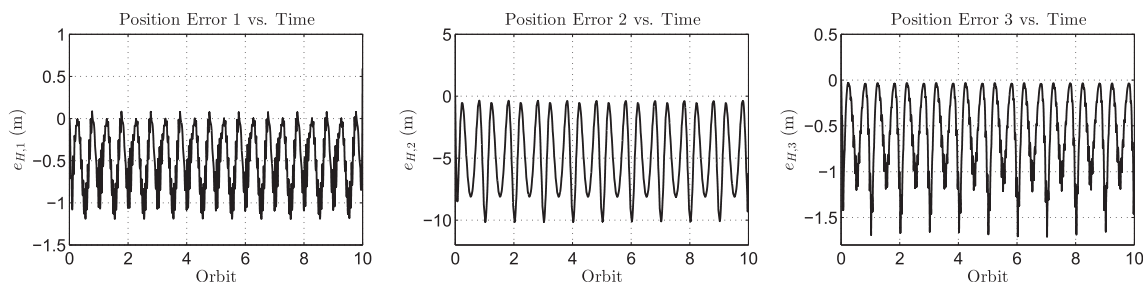

Fig. 7. Relative Position Errors with Non-Zero Off-set using 20-Impulse Hybrid LQR with Elliptic Ref.

Table 2

Performance, without Initial Off-Set, of Hybrid LQR based on Mean Differential Orbital Elements (from Ref. [14]) vs. Cartesian Coordinates (present).

Source	$|e_{H,1}|_{max}$	$|e_{H,2}|_{max}$	$|e_{H,3}|_{max}$	$|\Delta v|_{avg}$/orb	$\|\hat{q}\|_{10T}$	$|\hat{q}|_{max}$
Ref. [14]	2 m	~ 5 m	~ 8 m	0.4 mm/s	2.11e−5 C/kg	2.49e−4 C/kg
Present	1.2 m	10.1 m	1.7 m	0.22 m/s	1.43e−5 C/kg	4.44e−5 C/kg

can be achieved by increasing the number of impulses.

5. Conclusion

The hybrid LQR control approach of [12], based on differential orbital elements, was applied to a model constructed using a Cartesian description of relative position and velocity errors between spacecraft in formation. The control forces were assumed to consist of continuous Lorentz forces and impulsive thrusts, and the use of both circular and elliptic solutions as reference orbits was tested. In addition, J_2 perturbation effects were implemented in simulations, but not accommodated for by controller design.

Numerical simulation results were presented to demonstrate the superiority of using elliptic reference frames when the chief's orbit has a noticeable eccentricity. Furthermore, improvements obtained via complementing the Lorentz forces with impulsive thrusting was demonstrated, first by showing reduced errors and cost for the case of

initializing the deputy spacecraft on the desired PCO, and then by demonstrating significant control performance improvement for the case of non-zero initial off-set. The required specific charge and thrust Δv's were found to be reasonable. Comparison was also made against previous results in literature, namely those in Ref. [14].

Future work should study the practical issues in implementing the proposed controller in actual spacecraft, as well as the effects of modelling and sensing uncertainties. Closer examination of the consequences of changing the number and timing of the hybrid LQR controller's impulses is another possible venue for future work. Lastly, further improvements may result from accounting for the J_2 effects when designing the controller. To this end, analytic approximations to the solution of the gravitationally-perturbed equations of motions, such as Deprit's radial intermediary presented in Ref. [23] that performs a Lie transformation on the Hamiltonian to remove the short-periodic effects (the accuracy and efficiency of which has since been studied, such as recently in Ref. [24]), or similar intermediaries may be useful.

Appendix A. Nomenclature

Variables

C	rotation matrix between two frames
E	electrical field intensity (N/C)
$\mathscr{F}$	reference frame
$\mathscr{J}$	hybrid cost function
J_2	second order zonal harmonic
N	total number of impulses
P	Riccati solution
R	radius (m)
T	orbital period (s)
a	semi-major axis (m)
b	magnetic field vector (T)
e	relative state error
e	eccentricity
f	specific force vector (N/kg)
h	orbital angular momentum vector (m^2/s)
i	inclination (rad)
l	semi-latus rectum (m)
m	mass (kg)
n	mean orbital motion (rad/s)
q	electrostatic charge (C)
r	position vector (m)
v	velocity vector (m/s)
t	time (s)
t_0	time of perigee passage (s)
α	phase angle (rad)
θ	true anomaly (rad)
$\boldsymbol{\rho}$	relative position vector (m)
Ω	longitude of ascending node (rad)
μ	gravitational parameter (m^3/s^2)
$\boldsymbol{\nu}$	thrust impulse (N·s/kg)
Ξ	controllability Gramian matrix
$\boldsymbol{\omega}$	angular velocity vector (rad/s)
ω	argument of periapsis (rad)

Matrices

$1_{n \times n}$ an $n \times n$ identity matrix

$0_{m \times n}$ an $m \times n$ zero matrix

Operators

$\Delta(\cdot)$ variation (change) in a variable

$\delta(t)$ Dirac delta function

$\widehat{(\cdot)}$ normalized quantity

$\dot{(\cdot)}$ differentiation with respect to time

$|\cdot|$ Euclidean norm of a vector

$\| \cdot \|$ root mean squared norm of a quantity

$(\cdot)^{\times}$ skew-symmetric matrix operator

Subscripts

G in Earth-centred inertial frame

H in Hill frame

P in perifocal frame

c chief-related

d deputy-related

e earth-related

ct continuous-time

ds discrete-time

p perturbation

0 initial value

f final value

z corresponding to zero eigenvalue

nz corresponding to nonzero eigenvalue

avg average value of a quantity

max   maximum value of a quantity

pco projected circular orbit

ref reference

rel relative

nT computed over n orbital periods

Superscripts

$(\cdot)^{+}$ post-impulse quantity

$(\cdot)^{-}$ pre-impulse quantity

$(\cdot)^{*}$ optimal quantity

References

[1] M.A. Peck, Prospects and challenges for lorentz-augmented orbits, in: Proceedings of the AIAA Guidance, Navigation, and Control Conference and Exhibit, San Francisco, CA, Aug. 2005, http://dx.doi.org/10.2514/6.2005-5995.

[2] G.E. Pollock, J.W. Gangestad, J.M. Longuski, Analytical solutions for the relative motion of spacecraft subject to lorentz force perturbations, Acta Astronaut. 68 (1–2) (Jan.-Feb. 2011) 204–217, http://dx.doi.org/10.1016/j.actaastro.2010.07.007.

[3] G.W. Hill, Researches in the lunar theory, Am. J. Math. 1 (1) (1878) 5–26, http://dx.doi.org/10.2307/2369430.

[4] W.H. Clohessy, R.S. Wiltshire, Terminal guidance system for satellite rendezvous, J. Aerosp. Sci. 27 (9) (Sept. 1960) 653–658, http://dx.doi.org/10.2514/8.8704.

[5] M.A. Peck, B. Streetman, C.M. Saaj, V. Lappas, Spacecraft formation flying using lorentz forces, J. Br. Interplanet. Soc. 60 (Jul. 2007) 263–267.

[6] S. Tsujii, M. Bando, H. Yamakawa, Spacecraft formation flying dynamics and control using the geomagnetic lorentz force, J. Guid. Control, Dyn. 36 (1) (Jan.-Feb. 2013) 136–148, http://dx.doi.org/10.2514/1.57060.

[7] J. Tschauner, Elliptic orbit rendezvous, AIAA J. 5 (6) (1967) 1110–1113, http://dx.doi.org/10.2514/3.4145.

[8] T.E. Carter, New form for the optimal rendezvous equations near a keplerian orbit, J. Guid. Control, Dyn. 13 (1) (Jan.-Feb. 1990) 183–186, http://dx.doi.org/10.2514/3.20533.

[9] H. Schaub, S.R. Vadali, J.L. Junkins, K.T. Alfriend, Spacecraft formation flying control using mean orbit elements, J. Astronaut. Sci. 48 (1) (Jan.-Mar. 2000) 69–87.

[10] H. Schaub, K.T. Alfriend, j_2 invariant relative orbits for spacecraft formations, Celest. Mech. Dyn. Astron. 79 (2) (Feb. 2001) 77–95, http://dx.doi.org/10.1023/A:1011161811472.

[11] B.J. Streetman, Lorentz-augmented Orbit Dynamics and Mission Design, Ph.D. thesis, Cornell University, Ithaca, NY, Aug. 2008.

[12] L.A. Sobiesiak, Differential Orbital Element-based Spacecraft Formation Control Strategies, Ph.D. thesis, University of Toronto Institute for Aerospace Studies, Toronto, ON, 2014.

[13] G. Inalhan, M. Tillerson, J.P. How, Relative dynamics and control of spacecraft formations in eccentric orbits, J. Guid. Control, Dyn. 25 (1) (Jan.- Feb. 2002) 48–59, http://dx.doi.org/10.2514/2.4874.

[14] L.A. Sobiesiak, C.J. Damaren, Optimal continuous/impulsive control for lorentz-augmented spacecraft formations, J. Guid. Control, Dyn. 38 (1) (Jan. 2015) 151–157, http://dx.doi.org/10.2514/1.G000334.

[15] L.A. Sobiesiak, C.J. Damaren, Controllability of lorentz-augmented spacecraft formations, J. Guid. Control, Dyn. 38 (11) (Nov. 2015) 2188–2195, http://dx.doi.org/10.2514/1.G001148.

[16] X. Huang, Y. Yan, Y. Zhou, Optimal lorentz-augmented spacecraft formation flying in elliptic orbits, Acta Astronaut. 111 (Feb. 2015) 37–47, http://dx.doi.org/10.1016/j.actaastro.2015.02.012.

[17] Y. Ulybyshev, Long-term formation keeping of satellite constellation using linear-quadratic controller, J. Guid. Control, Dyn. 21 (1) (Jan.-Feb. 1998) 109–115, http://dx.doi.org/10.2514/2.4204.

[18] S.R. Vadali, S.S. Vaddi, K.T. Alfriend, An intelligent control concept for formation flying satellites, Int. J. Robust Nonlinear Control 12 (Feb. 2002) 97–115, http://dx.doi.org/10.1002/rnc.678.

[19] J. Pluym, C.J. Damaren, Dynamics and control of spacecraft formation flying: reference orbit selection and feedback control, in: Proceedings of the 13th Canadian Astronautics Conference (ASTRO 2006), Montreal, QC, Apr. 2006.

[20] A.H.J. de Ruiter, C.J. Damaren, J.R. Forbes, Spacecraft Dynamics and Control: An Introduction, Wiley, United Kingdom, 2013.

[21] J.R. Wertz, Spacecraft Attitude Determination and Control, D. Reidel Publishing Co., Dordrecht, Holland, 1978.

[22] S.S. Vaddi, S.R. Vadali, K.T. Alfriend, Formation flying: accommodating nonlinearity and eccentricity perturbations, J. Guid. Control, Dyn. 26 (2) (Mar.-Apr. 2003) 214–223, http://dx.doi.org/10.2514/2.5054.

[23] A. Deprit, The elimination of the parallax in satellite theory, Celest. Mech. 24 (2) (1981) 111–153, http://dx.doi.org/10.1007/BF01229192.

[24] P. Gurfil, M. Lara, Satellite onboard orbit propagation using deprit's radial intermediary, Celest. Mech. Dyn. Astron. 120 (2) (2014), http://dx.doi.org/10.1007/s10569-014-9576-1, 2017–2232.